Corrosion Science 126 (2017) 26–36

Contents lists available at ScienceDirect

Corrosion Science

journal homepage: www.elsevier.com/locate/corsci

Local supersaturation and the growth of protective scales during CO_2 corrosion of steel: Effect of pH and solution flow

Mobbassar Hassan Sk[a], Aboubakr M. Abdullah[a], Monika Ko[b,1], Bridget Ingham[c], Nick Laycock[d], Rakesh Arul[e], David. E. Williams[e,*]

[a] Center for Advanced Materials, Qatar University, P.O. Box 2713, Doha, Qatar
[b] Quest Integrity Group, P.O. Box 38-096, Lower Hutt 5045, New Zealand
[c] Callaghan Innovation, PO Box 31-310, Lower Hutt, New Zealand
[d] Qatar Shell Research and Technology Centre, P.O. Box 3747, Doha, Qatar
[e] School of Chemical Sciences and MacDiarmid Institute for Advanced Materials and Nanotechnology, University of Auckland, Private Bag 92019, Auckland, 1022, New Zealand

ARTICLE INFO

Keyword:
CO_2 corrosion
hydrodynamic effects
electrocrystallisation
siderite
chukanovite
passivation

ABSTRACT

By correlating *in-situ* synchrotron X-ray diffraction measurements with electrochemical measurements using a rotating disc electrode, we demonstrate the critical dependence on the local supersaturation of the kinetics of formation of a protective crystalline scale on the surface of carbon steel during CO_2 corrosion in brine at elevated temperature. We show that the total current is the sum of a current due to dissolution of iron and a current due to growth of a crystalline layer. We show that the dissolution current and the surface supersaturation are controlled by the thickness of an initially-formed amorphous layer. As in earlier work at room temperature, we infer that the amorphous layer dissolves as a carbonato-iron complex with surface concentration of the dissolving species determined by the electrode potential, and speculate on the importance of the chemistry of this dissolution reaction in determining the corrosion result. We construct a simple transport-reaction model, which shows that the supersaturation is determined by the precipitation rate constant of colloidal $FeCO_3$ and by the product of the current for Fe dissolution and the diffusion boundary layer thickness. Using this model, we show crystal growth rate varying quadratically with supersaturation at pH 6.8 and linearly at pH 7.3. The effects of electrode potential, surface roughness, microstructure and flow are simply to change supersaturation by changing the current density per unit projected area flowing through the amorphous initially formed layer. Variation of brine concentration has no effect. We illustrate the sensitivity to solution flow of the crystallinity of the final scale. We show that siderite is the first crystalline product and that chukanovite follows, with a delay time that decreases with increasing pH. The ratio of chukanovite to siderite is low at sufficiently high pH and increases with decreasing pH, possibly through a maximum. From the results, we advance ideas concerning the importance of local microenvironments and local fluctuations in mass-transport rate.

1. Introduction

As a result of its importance in oil and gas wells and pipelines, the CO_2 corrosion of carbon steel has been extensively studied [1]. The various models for the corrosion rate, important for pipeline corrosion management, agree moderately well in non-scaling conditions, but diverge under conditions where an iron carbonate scale forms [2,3]. At temperatures above about 70–80 °C, CO_2 pressures greater than about 0.5 bar and pH greater than about 6, extremely protective crystalline siderite ($FeCO_3$) scales form, that cause diminution of the corrosion rate to low values [1,3]. This effect is incorporated in empirical models using a 'scaling factor' [2]. Other models attempt to compute the corrosion rate from first principles [4,5] but cannot correctly *a-priori* incorporate the effect of the formation of the scale because the necessary rate parameters describing the nucleation and growth of the scale are not reliably known [6]; such models therefore fail for scale forming conditions [2]. The work in [7] aimed to fill this gap, developing a numerical model to describe the formation kinetics and growth morphology of the surface layer. The scaling factor or "surface scaling tendency" was expressed as a ratio of the precipitation rate of $FeCO_3$ to

* Corresponding author.
E-mail address: David.williams@auckland.ac.nz (D.E. Williams).
[1] Present address: Quest Integrity Group, B-20-UG Jalan C180/1, 43200 Cheras, Selangor, Malaysia.

http://dx.doi.org/10.1016/j.corsci.2017.05.026
Received 17 January 2017; Received in revised form 6 May 2017; Accepted 29 May 2017
Available online 03 June 2017
0010-938X/ © 2017 Elsevier Ltd. All rights reserved.

the corrosion rate. The precipitation rate and its relationship to the supersaturation of $FeCO_3$ and then to porosity of the developing scale is the important element of this model, and some empirical fitting was used to develop relationships that predicted experimental results. If the solution was significantly supersaturated with $FeCO_3$ at the start of an experiment, presumably ensuring that the scale was nucleated from the start, then modelling the decrease of corrosion rate with time as a crystalline scale spreads over the surface was successful [7]. The crystal growth of siderite from solution is surface reaction rate-controlled. It is strongly temperature-dependent, strongly pH-dependent and slow [8]. The formation of a protective scale thus requires a sufficiently high temperature, a sufficiently high pH, a significant supersaturation [7,9] and the time-scale for its formation is long. These factors appear to be important in the initiation of mesa corrosion, resulting when the scale is damaged and the repair is slow [3,9]. We have addressed the *in-situ* measurement of scale growth and its effect on corrosion rate using synchrotron X-ray diffraction (XRD) and small-angle X-ray scattering. We have shown that the formation of crystalline siderite is slow and requires a significant supersaturation of the solution, which is sensitive to the concentration of other metal ions in solution, particularly higher-valent ions such as Cr^{3+} which may be added to the solution or derived from the steel. Chukanovite − $Fe_2(OH)_2CO_3$ is also formed as a crystalline product [10–15]. Others have shown at lower temperature (45 °C) and pH 6 the formation of chukanovite and magnetite [16].

The flow rate of fluid is important in influencing corrosion rate of oil & gas tubulars. In oil pipelines it has a significant impact on whether or not the steel walls are 'water wet', because higher velocities tend to support entrainment of water droplets within the oil. In gas pipelines the higher velocities create 'annular dispersed' flow in which the entire pipe circumference is water wet. Then, where the walls are indeed water wet, the flow rate controls the transport of reactants (e.g. CO_2) to the corroding surface and corrosion products (e.g. Fe^{2+} ions) away from the surface. It is in this 'water-wet' condition that the presence or otherwise of a siderite scale, and its morphology, become of importance in determining the corrosion rate.

Now, the critical role of the supersaturation in controlling the kinetics of crystallization would imply some effect of solution flow on the formation of a protective scale. Note that this effect is distinct from any mechanical effects on scale stability caused by high solution flow rates. In this, the literature seems to offer divergent results. Some reports describe that this protective scale forms even under high liquid flow rates [17], whilst other flow loop experiments at high flow rates can show no protective scale formation [18], even under conditions where a scale might be expected [19]. De Moraes et al. described a critical condition for transition between protective and non-protective scales [20] as part of which increase of flow velocity could have an important effect. At sufficiently high temperature (93 °C) and pH, a thin, compact, adherent and protective corrosion scale was formed and an increase of solution flow velocity had only a minor effect on corrosion rate. The development of this scale could be followed by polarisation resistance measurements, which showed a sharp increase after about 50 h of exposure. At lower pH, a thick and porous, partially protective scale was formed. Increase of flow rate in this case could transform the situation from one where a partially protective scale was present to one where no protective scale was present. When this happened, localized corrosion could also be triggered. The boundary between protective, flow-insensitive state and partially-protective, flow-sensitive state was dependent on pH, temperature and CO_2 partial pressure. Nesic et al. similarly showed a subtle difference in effect of the type of flow − straight pipe or rotating cylinder − on whether a dense siderite film was formed or whether the metal simply dissolved, leaving a porous Fe_3C mass; pH and temperature were again important factors in determining whether the different flow regimes gave different results [21].

Because of this apparent sensitivity of scale formation to subtle effects of solution flow rate, and because the corrosion rate of steel in CO_2-saturated brine at elevated temperature is critically dependent on whether or not a protective crystalline corrosion scale is formed, in the present paper we focus on the effect of flow on the initial formation kinetics of crystalline scales. By correlating *in-situ* synchrotron X-ray diffraction measurements with electrochemical measurements using a rotating disc electrode, we demonstrate the critical dependence on the local supersaturation of the kinetics of formation of a protective crystalline scale on the surface of carbon steel during CO_2 corrosion in brine at elevated temperature. We show that the formation of a protective scale occurs by a direct electrochemical reaction of the steel, an electrocrystallisation reaction, occurring in parallel to a dissolution reaction. This dissolution reaction has previously been shown to result in a colloidal product [12]. Earlier work at room temperature has shown dissolution catalysed by bicarbonate, and has inferred an unstable, soluble carbonato complex of iron as the product [22,23]. The catalysed dissolution reaction occurs through a species that has a surface concentration controlled by the electrode potential. The thickness of a thin, amorphous surface film controls the current both for the dissolution reaction and the electrocrystallisation reaction. The existence of this 'prepassive' film has been deduced electrochemically by others and detected ellipsometrically albeit at room temperature and at higher pH than we have studied here [23,24]. We further deduce that there is a second, parallel dissolution path that is not flow rate-dependent and which is of importance in determining the flow rate-dependence of the surface supersaturation. We show that the formation of chukanovite follows that of siderite and is pH-sensitive. Overall, this is a complex system. We speculate on the consequences for corrosion of the kinetics of the various interconnected processes.

2. Experimental

2.1. Materials

Three different steel samples were used in this study: API J55 and API 5CT L80 pipeline steels and AISI 1006 low carbon steel. The API J55 and AISI 1006 steel samples had ferritic/pearlitic microstructure and the API L80 steel samples had a tempered martensitic microstructure. The chemical compositions are shown in Table 1. The API J55 and API L80 steel samples were machined from a pipeline sample to produce round bars of diameter 6 mm which were then customized to be used as rotating disk working electrodes (RDE). The samples were cut to 15 mm length pieces which were then inner-threaded from one end, ultrasonically cleaned with *n*-butane for 10 min, washed with distilled water and dried. The samples were then mounted using epoxy resin into a PTFE shield (see Supporting Information, SI) and unless otherwise stated, the exposed surface was ground to a 15 µm surface finish using silicon carbide paper.

Table 1
Steel chemical compositions.

Steel samples	Wt.% (and Fe bal.)										
Composition	C	Si	Mn	Cr	Mo	S	P	Ni	Cu	Al	V
J55	0.29	0.33	1.30	0.06	0.04	0.001	0.009	0.02	0.02	–	0.001
L80	0.25	0.20	0.9	0.07	0.03	0.005	0.014	0.06	0.14	0.01	< 0.01
AISI 1006	0.06	0.04	0.30	0.05	< 0.01	0.019	0.012	0.06	0.16	< 0.01	< 0.01

2.2. Test solution

The base test solution for all experiments was 0.5 M NaCl, deaerated and saturated with CO_2 by bubbling for at least 1 h a stream of high-purity CO_2 gas (supplier specification < 4 ppm O_2) at 1 bar. The pH was altered by adding measured amounts of 2 M NaOH (SI: table S1), measured at room temperature with a laboratory pH meter and calculated at elevated temperature based on the equilibrium of ionic species in the solution with carbon dioxide at fixed partial pressure (data sources for carbonate equilibrium constants, water vapour pressure, Henry's law constant for CO_2 and activity coefficients in aqueous NaCl as a function of temperature given in [11]. An example calculation is given in the SI.). This procedure was repeatable and reliable and avoided possible errors associated with the temperature correction of laboratory pH meters and temperature dependence of the reference element of combination pH electrodes. Unless otherwise stated, experiments were conducted at 80 °C and the calculated pH was varied between 4.2 and 7.3. Over this range $pH_{calc,80C} - pH_{measured,RT} \approx +0.5$. Dissolution of Fe could cause a pH change. However, room temperature pH measurement before and after an experiment showed change < 0.01 pH.

2.3. Reference electrodes

Measurements were made in three different laboratories (synchrotron, NZ, Qatar) spanning some years and using different reference electrodes. Consistency of potential scales was checked as follows. Reference electrode potentials are strongly temperature-dependent [25,26], and with commercial electrodes there is a possible issue that, at elevated temperature the reference solution is not saturated in AgCl. In the laboratory cells, the reference electrode – two different setups, one with Ag,AgCl/sat. KCl and the other with saturated calomel electrode – was mounted externally and connected to the cell via a Luggin capillary containing the test solution. The temperature of the external reference electrode was measured to be around 40 °C. The correction to the reference electrode at room temperature is +10 mV [26]. In the synchrotron cell the reference electrode (Ag,AgCl/3 M KCl) was immersed directly in the hot sample solution. The potential of the microreference electrode used in the synchrotron experiment was measured with respect to another Ag,AgCl/3 M KCl reference electrode at room temperature, connected to the heated solution by an electrolyte bridge of the same composition as the sample solution. For this comparison, the thermal junction potential in the electrolyte bridge was ignored. The initial potential difference of the reference electrodes was 1.2 mV and the potential drift was less than 4 mV in 1.5 h. Unless otherwise stated, potentials have been quoted with respect to the corrosion potential of the steel in the test solution: Table 2 shows corrosion potential values. These were consistent across all experiments in all three laboratories.

2.4. Electrochemistry flow (RDE) experiments

The apparatus is shown in the SI. The electrochemical tests were carried out in a 1 L double jacketed glass cell. Water was circulated through the outer jacket of the cell at a constant temperature. The experiments were controlled using a Gamry 600 Potentiostat. The counter electrode (CE) was a Pt wire ring in the plane of, and centred on the working electrode (WE). As noted above, the Ag,AgCl/sat KCl reference electrode was held externally and connected to the cell via Luggin capillary containing the test solution; the tip of the capillary was centred on the WE. The RDE was controlled using a Gamry RDE710 Rotating Electrode regulator. The experimental sequence was: (a) a potential of −1 V (*vs.* Ag/AgCl saturated KCl) was applied to the sample for 5 min to reduce air-formed surface oxides; (b) the open-circuit potential (OCP) was recorded until an apparent steady-state was reached (approximately 3–5 min). Once the desired condition was achieved, the CO_2 gas bubbler inlet was switched to the gas blanket arrangement; (c) an anodic potentiostatic step was applied to a fixed potential with respect to OCP and the resulting current density signal was recorded. Experiments were conducted at either fixed RDE rotational speed throughout the measurement, or stepping the rotation rate from high to low value and back again, each step being held for 1 min. Throughout the experiment, the cell was sealed to prevent oxygen ingress, and CO_2 was bubbled or blanketed continuously.

Table 2
Open circuit corrosion potentials with respect to Ag,AgCl/sat KCl at 40 °C: steel in CO_2–saturated 0.5 M NaCl at 80 °C.

pH_{calc}	J55	L80	AISI 1006 (from Fig. 1)
4.6	−665 to −675	−660 to −670	−670
6.8	−700 to −710	−695 to −705	−675
7.3	−710 to −720	−705 to −715	−695

2.5. Synchrotron X-Ray diffraction experiments

In situ synchrotron XRD experiments were conducted at the Powder Diffraction beam line at the Australian Synchrotron, as previously described [10]. The working electrode was a 1.5 mm diameter AISI 1006 steel rod, embedded in epoxy resin with the top face polished to 1 μm surface finish. A Pt counter electrode and Ag,AgCl/3 M KCl microreference electrode were used. The X-ray beam energy was 15 keV (i.e. λ = 0.82400 Å) and the beam size was 0.2 mm × 0.7 mm (vertical × horizontal). Diffraction images were recorded using a MarCCD 165 detector (apparent pixel size 79 μm) located 137 mm distance from the WE. The exposure time for each image during the *in situ* measurements was 1 min, with 3–4 s readout time. X-rays were incident on the polished surface of the WE at a grazing angle (< 1°).

The X-ray diffraction data were processed as described in the previous work [10,11,13–15,27]. The diffraction data were fitted using a Gaussian peak function to obtain the peak areas. The integrated X-ray diffraction intensity for the (*hkl*) reflection (peak) of phase *A*, $I_{hkl,A}$, is proportional to:

$$I_{hkl,A} \propto C_0 \cdot w_A \cdot L \cdot P \cdot m_{hkl,A} \cdot T_{hkl,A} \cdot \frac{|F_{hkl,A}|^2}{{V_A}^2} \cdot a \exp(-2M)$$

where C_0 is a constant (depending on the incident intensity and other factors); w_A is the mass of phase A; L is the Lorentz factor and P is the polarisation factor, both of which are dependent on the scattering angle 2θ and are the same for all phases. $m_{hkl,A}$, $T_{hkl,A}$, and $F_{hkl,A}$ are the multiplicity factor, the texture factor, and the structure factor for the (*hkl*) reflection of phase A respectively; V_A is the unit cell volume of phase A; a is the illuminated sample area. The Debye-Waller factor 2M relates to the root-mean-square displacement disorder and is dependent on the scattering angle[28,29].

The geometrical terms C_0, L, P, a and exp(–2M) are the same for all phases and can be combined as a single constant providing the scattering angles of the selected reflections are reasonably close in 2θ. Since the material is isotropic, $T_{hkl,A} = 1$ for all reflections. Theoretical values for the terms $m_{hkl,A}$, $F_{hkl,A}$ and V_A are known, leaving the mass of each phase as an unknown that can be extracted based on relative peak intensities. In order to compare one experiment with another (where C_0 and a may not necessarily be the same) the integrated siderite (104) and chukanovite (021) peak intensities were first normalized to the initial integrated intensity of the Fe (110) peak, since this is the only phase present at the start of the experiment. Then, the normalized siderite and chukanovite peak areas were multiplied by the conversion factors 7.57 and 16.2 respectively to give relative masses. Conversion from mass to volume is performed by dividing by the density of the material (crystallographic density of siderite/chukanovite = 1.1).

3. Results and discussion

In section 3.1, we present the general features of potentiostatic transients, extending the previous work to cover a range of pH and solution flow rate. Then, we dissect the transient into its component parts, which we identify as an electrocrystallisation reaction, forming a crystalline $FeCO_3$ layer (Eq. (1)) and a dissolution reaction leading to colloidal $FeCO_3$ (Eq. (2)). We do this by first fitting the growth of the crystalline layer, measured by *in-situ* X-ray diffraction, to the Avrami expression (section 3.2). We show that siderite nucleates immediately upon application of the anodic potential whilst chukanovite forms with a pH-dependent delay. We show that the crystal growth rate constant correlates with the time to achieve the current peak in the potentiostatic transient, and hence deduce that the time to the peak in other experiments can be used to uncover the dependence of the crystal growth rate constant on electrode potential and rotation rate.

$$Fe(s) + CO_3^{2-}(aq) \rightarrow FeCO_3(crystalline) + 2e^- \quad (1)$$

$$Fe(s). \rightarrow Fe^{(II)}(aq) + 2e^-;\ Fe^{(II)}(aq) + CO_3^{2-}(aq) \rightarrow FeCO_3(colloid) \quad (2)$$

Then, in section 3.3, we show that if we consider the crystal formation as an electrochemical reaction (Eq. (1)), by following classic studies of electrocrystallisation using the Avrami equation for the electrochemical reaction rate we can indeed satisfactorily decompose the total current into a part due to Eq. (1) and a part due to Eq. (2). Thus, we do not need any special hypothesis regarding changes in the interface (such as are suggested in [11,12]) to explain the current peak. We are then, in section 3.4, able to examine the dependence of the dissolution process (Eq. (2)) on pH and electrode potential. We deduce the presence of a thin film, which was undetectable by *in-situ* X-ray diffraction and which we assume to be an amorphous ferrous carbonate, which controls both the dissolution rate and the electrocrystallisation rate through control of ion transfer from metal to the film-solution interface. We then examine in detail the effects of the electrode rotation rate to deduce more information concerning the chemistry of the dissolution reaction (Eq. (2)). We show that the dependence of the electrocrystallisation reaction rate on the surface supersaturation rationalises the effects of rotation rate, pH and surface roughness on this process. We develop theory showing how the surface supersaturation is dependent on the transport rate, the dissolution rate and on the precipitation rate of colloidal $FeCO_3$. We are then able to offer some comments on how the different parts of this complex process separately impact observed corrosion.

3.1. General features of potentiostatic transients

The general features of the potentiostatic transients under static conditions are illustrated in Fig. 1. As previously described [10–15] and consistent with earlier work[30,31], following the potential step from the open-circuit potential, the current density decreases rapidly to a plateau. After some time, it then rises to a peak before decaying to a low value. We have previously shown that the rise to the peak corresponds to the detection by *in-situ* diffraction of crystalline $FeCO_3$ on the surface and have speculated that the effect is due either to a local pH change caused by consumption of carbonate releasing H^+, or to the growing crystals consuming and cracking an amorphous layer that is present on the surface [11,12]. Whilst these explanations might have some relevance, later in the present paper we develop a much simpler idea. The magnitude of the current peak increases with increasing electrode potential and the time to the current peak, t_{peak}, decreases. The pre-peak plateau current density, i_{plat}, shows approximately a Tafel relationship with change of electrode potential. The Tafel slope decreases with decreasing pH. The corrosion potential decreases with increasing pH. With decreasing pH, the current i_{plat} and the time t_{peak} both increase. At sufficiently low pH, a current peak is no longer observed within the timescale explored here. The effects of varying rotation rate are illustrated in Fig. 2. The pre-peak plateau current density, i_{plat}, and the time to the current maximum, t_{peak}, both increase with increasing electrode rotation rate. The shape of the current peak also changes, becoming broader with increasing rotation rate. The magnitude of the current at the peak increases then decreases as rotation rate increases. With decreasing electrode potential, i_{plat} decreases and t_{peak} increases (see later). After 1hr of total exposure, the surface was completely covered with a microcrystalline layer as previously shown[10]. In addition, large, well-formed crystals become more prominent on the surface with increasing rotation rate (see also Fig. S5). *Ex-situ* powder diffractometry identified siderite.

3.2. In-situ X-ray powder diffraction: crystal growth rate and correlation of time to current peak with rate constant for crystal growth

In situ synchrotron X-ray powder diffraction was used to monitor the formation of crystalline phases on the steel surface during CO_2 corrosion. We have previously shown [14] that the crystal growth rate is sensitive to stirring of the electrolyte. In these experiments however, the hydrodynamics were ill-controlled and very different to the conditions pertaining at the rotating disc electrode. The crystal growth may however be described quantitatively using the theory of Avrami [33]:

$$V = V_m\{1 - \exp[-(k_{Avrami}(t - t_d))^n]\} \quad (3)$$

Where, V denotes the crystal volume (V_m at full coverage). The exponent, n, depends upon the crystal shape and whether the crystal nucleation is "instantaneous" (i.e. all nuclei start growing at (t- t_d) = 0) or "progressive" (i.e. the number of growth nuclei increases in time). The rate constant, k_{Avrami}, for instantaneous nucleation reflects the rate constant for crystal growth from the nuclei, and for progressive nucleation reflects the product of the time-dependent nucleation probability and the rate constant for crystal growth. The time delay, t_d, accounts for the possibility of an induction time before the nucleation of crystals commences.

Fig. 3a shows the relative crystal volume derived from the *in situ* synchrotron X-ray powder diffraction data and a typical fit to the Avrami model for siderite growth under semi-static conditions, with time delay t_d = 0. Fig. 3a shows the effect on the fit of allowing n to vary freely (n = 1.92 was found to give the best fit), and of fixing n = 3 (corresponding to instantaneous activation of seed nuclei and polyhedral crystal growth, or progressive plate-like growth with density of growth nuclei increasing linearly with time). The derived rate constant, k_{Avrami}, does not depend on the choice of n. So, the current peak can be identified as a part, i_{cryst}, of the total current that is due to the formation of a crystalline film: $i_{cryst} \propto dV/dt$ [34,35]. In that case, the current maximum for t_d = 0 would be expected at a time, t_{peak} such that: $k_{Avrami}t_{peak} = \sqrt[n]{1 - 1/n}$. Fig. 3b shows that indeed the reciprocal time to the current peak in these experiments, $(t_{peak})^{-1}$, correlates well with the rate constant for siderite growth. It is noticeable that, in the synchrotron cell (semi-static solution; long diffusion path) the time-scales required for nucleation of crystalline siderite were significantly longer, and the electrode potential needed was significantly more anodic, than for the laboratory cell.

The full set of fitted parameters is given in the supporting information, Table S2. For siderite, time delay t_d is equal to 0 under all conditions explored. For chukanovite (Fig. 4), t_d increased with decreasing pH and with decrease of electrode potential. Following the delay time, however, the rate constant for growth of chukanovite as observed in the synchrotron experiments was not significantly different to that for siderite. The ratio of chukanovite to siderite at full coverage showed an apparent maximum with pH. Our previous work [14] indicated that at pH 6.8, the volume at full coverage, V_m, for chukanovite varied with stirring of the solution whereas for siderite it did not. There was no obvious pattern in the variation of n (dependent on crystal shape and nucleation pathways), which lay between 2 and 4 for both phases.

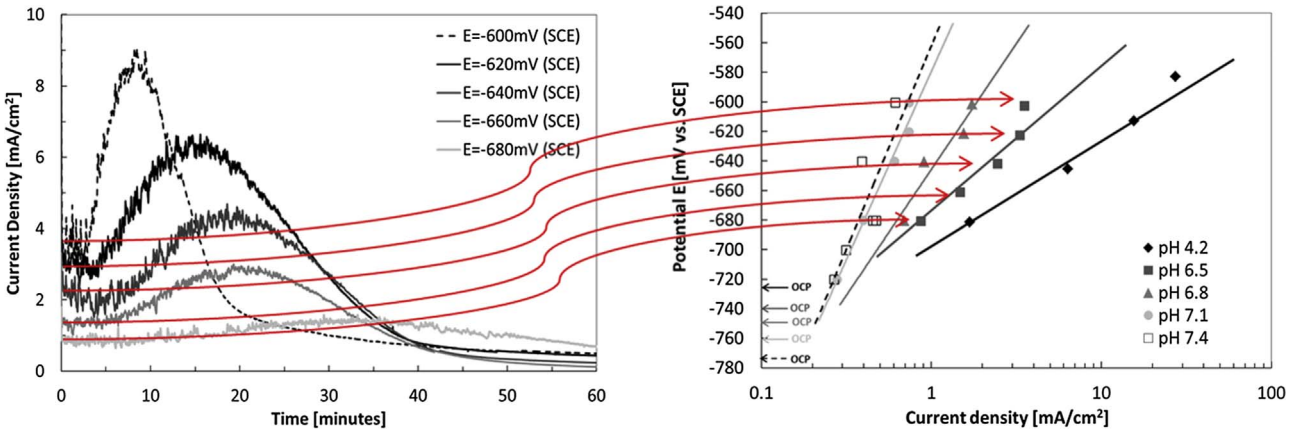

Fig. 1. Potentiostatic transients with varying electrode potential and pH_{calc} in CO_2–saturated 0.5 M NaCl at 80 °C, with stirring by CO_2 bubbling only, for AISI 1006 steel. (A): pH_{calc} 6.5; (B) Tafel dependence of i_{plat}. The electrode potential, E, was measured with respect to an SCE reference electrode at approx. 40 °C ($E_{calomel} - E_{Ag,AgCl(satKCl)} = +71$ mV at 40 °C [26,32]).

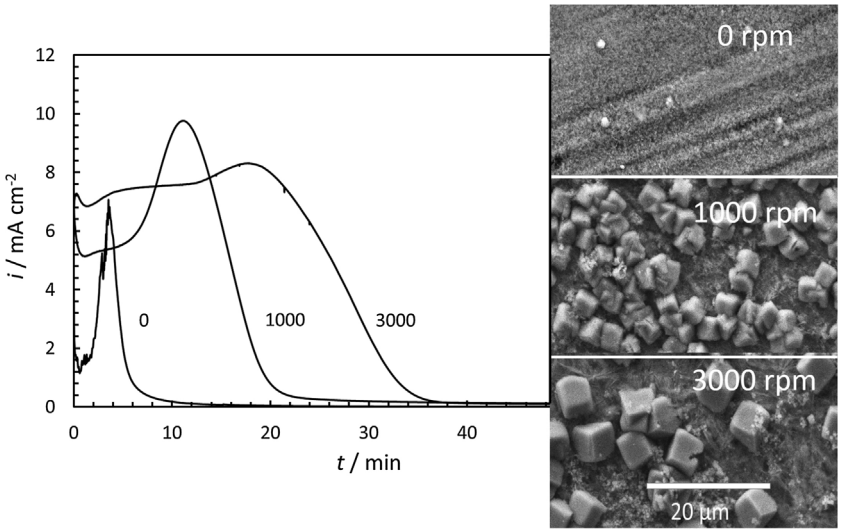

Fig. 2. Effect of varying electrode rotation rate (curve label: rpm) on potentiostatic transients. E-E_{corr} = +150 mV, for J55 carbon steel in CO_2–saturated 0.5 M NaCl at 80 °C and pH_{calc} = 6.8. The images show the surface appearance when the specimen was removed from the solution after 1 h of polarisation (scale bar 20 µm, applicable to all images).

In view of the results presented below, on the supersaturation-dependence of crystallization, and given that the mass transport in the synchrotron cell was not well-controlled, it is likely that there was a significant variability in growth rate, crystal form and probability of crystal nucleation linked to changes in local conditions at the electrode.

The observation of a delay time for chukanovite indicates that formation of this phase follows that of siderite. For open-circuit corrosion under a sand deposit, in a solution of 0.01 wt% $NaHCO_3$ containing a corrosion inhibitor, saturated with CO_2 at 80 °C (pH_{calc} ~5.1), Pandarina et al. [36] show chukanovite as the dominant corrosion product and show micrographs interpretable as showing siderite transforming into chukanovite. At higher pH, only siderite was formed under a sand deposit [37].

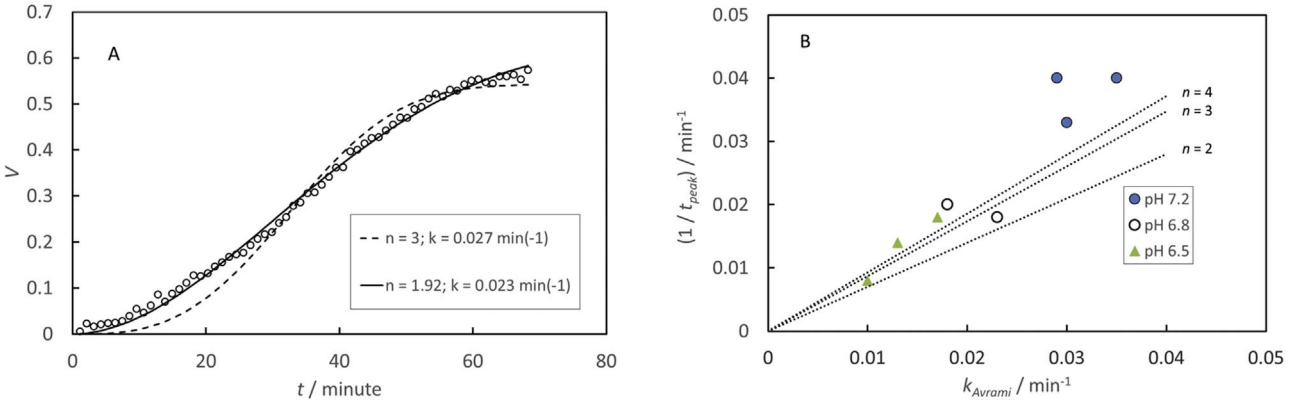

Fig. 3. Avrami model for evolution of crystalline siderite, fitted to *in-situ* diffraction data. (A): relative crystal volume, V, against time, t, for AISI 1006 steel in CO_2–saturated 0.5 M NaCl at 80 °C and pH_{calc} = 6.8, E-E_{corr} = +200 mV, fitted with $t_d = 0$ in Eq. (1) (B) Reciprocal time to current peak, $(t_{peak})^{-1}$ against Avrami rate constant, k_{Avrami} for *in-situ* diffraction experiments at E-E_{corr} = +140, +160 and +200 mV at different pH_{calc}. The lines are the expected correlation for particular values of n if the current peak is accounted for by growth of a crystalline film that spreads to cover the surface according to Eq. (3).

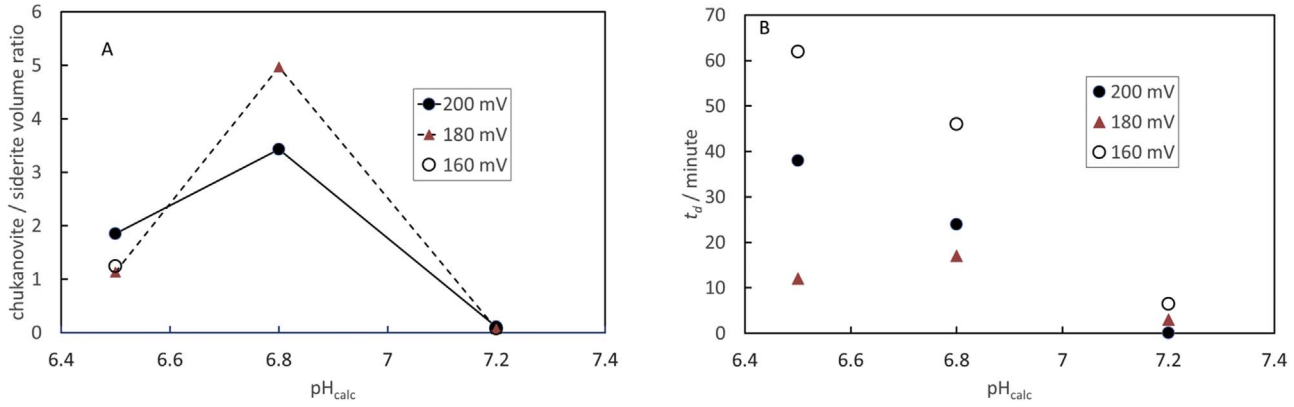

Fig. 4. (A) Final volume ratio of chukanovite to siderite; and (B) delay before commencement of chukanovite crystallization, t_d as a function of calculated solution pH (CO_2–saturated 0.5 M NaCl at 80 °C) for different $E - E_{corr}$.

3.3. Total current is the sum of current due to dissolution and current due to formation of crystalline product

In previous work [10,12], the results of *in-situ* synchrotron XRD and small- and wide-angle X-ray scattering (SAXS-WAXS) showed that the formation of the crystalline product was preceded by significant anodic dissolution of the iron, which resulted in the roughening of the steel surface and the formation of a colloidal precipitate in the solution. So, here we express the total current as the sum of current due to dissolution and current due to formation of crystalline product. The current due to formation of the crystalline product is, as noted above, $i_{cryst} \propto dV/dt \propto Vt^{n-1}$. We assume that the dissolution current, i_{diss}, is proportional to the area not covered by the crystalline product and can be written as an approximation: $i_{diss} = i_{diss,0}(1 - V/V_m)$, where $i_{diss,o}$ signifies the initial value of the dissolution current. Then the total current can be expressed as the sum $i = i_{diss} + i_{cryst}$ with fitting parameters the proportionality constant for i_{cryst}, n, k_{Avrami} and $i_{diss,0}$. Fig. 5 illustrates the result, which is satisfactory. Given the simplification implicit in the assumption of n constant and of growth habit uniform throughout the current transient, and taking account of the experimental variability, we simply take $k_{Avrami}t_{peak} = 1$ and assume that in the electrochemical experiments with the rotating disc, $(t_{peak})^{-1}$can be used as an estimate for the crystal growth rate constant. The error is not so large as to significantly bias the results, as is evident from Fig. 3.

3.4. Pre-peak plateau current and initial surface film

Fig. 5 shows that the pre-peak plateau current, i_{plat}, can be identified to a reasonable approximation with the initial dissolution current. The Tafel slope, b_{plat}, for the plateau current, i_{plat}, strongly increases as pH increases, for pH greater than about 6 (Fig. 6). The Tafel slope was determined both from measurements of the plateau current in the full potentiostatic transient at constant E, as in Fig. 1, and also by stepping the potential during the plateau part of the transient: see Fig. S3. At pH$_{calc}$ = 7.3, the current was not stable: the system was not in a steady state on the time scale of the experiment and the derived Tafel slope was very variable. At lower pH, the current in the plateau region at short enough time (ie before the contribution of i_{cryst} became too high) was reasonably stable.

The behaviour can be rationalised with a model in which dissolution occurs through a thin surface film, undetectable by the X-ray measurement, which forms rapidly following the potential step from open-circuit and whose growth causes the initial current decrease, down to the plateau, immediately following application of the anodic potential. A plateau current implies that this surface layer comes to a constant thickness during this phase of the experiment. Dissolution through a 'prepassive' film has been deduced previously for this system at room temperature and somewhat higher pH [23,24]. The decomposition of the current into two parts, shown in Fig. 5, further illustrates that the dissolution current is constant during most of this phase of the transient before i_{cryst} starts to increase. The potential difference between metal and solution, that drives the dissolution, is the sum of that across the film, $\Delta\phi_{film}$, and that across the two interfaces, $\Delta\phi_{mf}$ for the metal-film interface and $\Delta\phi_{fs}$, for the film-solution interface. The current density might in limits of low- and high-current density vary exponentially or linearly with each of these potential differences, depending on their magnitude.

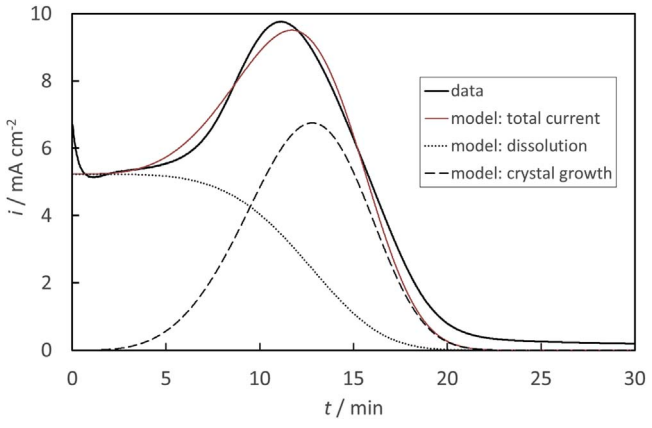

Fig. 5. Decomposition of total current into a part due to dissolution and a part due to growth of a crystalline layer (Eq. (3)). Data from Fig. 1: E-E_{corr} = +150 mV, for J55 steel in CO_2–saturated 0.5 M NaCl at 80 °C and pH$_{calc}$ = 6.8; electrode rotation rate 1,000 rpm.

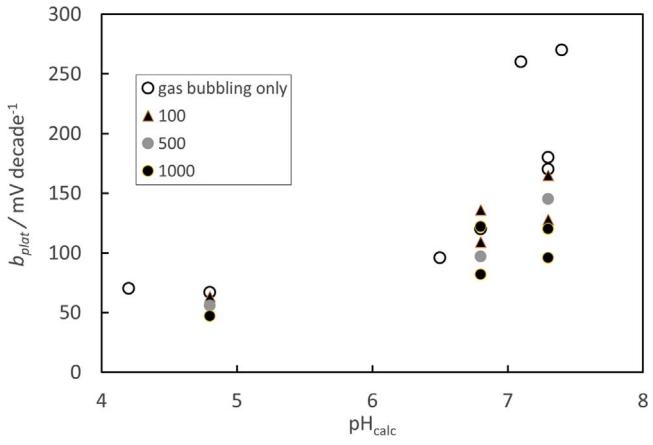

Fig. 6. Tafel slope for electrode potential-dependence of pre-peak plateau current, b_{plat}, as a function of solution pH; carbon steel in CO_2–saturated 0.5 M NaCl at 80 °C. Legend: electrode rotation rate/rpm.

If the film thickness is h, then one illustrative case is if one of the interface potential differences is much smaller than the other and varies logarithmically with current density with Tafel slope, b. If the film behaves as a simple resistor so $\Delta\phi_{\text{film}} = hi/\sigma$ where σ denotes the conductivity of the film; then

$$b_{plat} = b + hi/\sigma \tag{4}$$

The observed b_{plat} would be an apparent Tafel slope averaged over a range of potential. It could appear to be approximately constant if the range of i is not too large, or if the variation of film thickness with current density is such that $hi \sim$ constant. The results in Fig. 6 imply that h/σ increases significantly with increase of pH above about pH 6. These deductions are consistent with the presence of some sort of thin carbonate film through which iron is dissolving to create colloidal material in solution, as we and others have previously surmised [12,22–24]. The current is constant because the surface layer thickness adjusts such that the rates of dissolution and formation of the surface layer are equal.

3.5. Apparent surface supersaturation from rotation rate-dependence of i_{plat}

In the initial plateau region, the current changes essentially immediately in response to change of rotation rate, and provided that the current rise towards the peak has not commenced, the current responds to changes in rotation rate essentially without hysteresis (see Fig. S4). Fig. 7 shows that the rotation rate dependence of current follows the Levich equation for diffusion to a rotating disk electrode, with a potential-dependent offset denoted $i_{diss,n}$:

$$i_{plat} = k_m\omega^{\frac{1}{2}} + i_{diss,n} = i_{diss} + i_{diss,n} \tag{5}$$

Where i_{diss} denotes the transport-dependent part of the current, k_m is the Levich constant, ω is the angular rotation rate of the electrode (rad s^{-1}) and $i_{diss,n}$ the potential dependent offset (mA cm^{-2}). The steels of different microstructure are identical in their behavior. This behavior is the same as that reported for iron dissolution in bicarbonate buffer at ambient temperature [23].

A straightforward model for Eq. (5) follows from the separation of the current into a transport-dependent and a transport-independent part. For the for the transport-dependent part we assume that in the steady state, dissolution of the pre-peak film occurs with a surface concentration, c_s, of a dissolving species (whose nature is to be determined) that is fixed by the electrode potential. In the steady state, the current due to reaction 2 will equal the flux away from the surface of the dissolving species. That is, $i_{diss} = zFDc_s/\delta$ where δ denotes the diffusion boundary layer thickness, z the charge number for the dissolving species and c_s its concentration at the film-solution interface. D is the diffusion coefficient for the dissolving species. With the assumption of steady state conditions, the Levich constant, k_m, for the rotating disc arrangement is:

$$k_m = zFDc_s/\delta\omega^{1/2} = zF(0.621c_s\nu^{-1/6}D^{2/3}) \tag{6}$$

where ν is the kinematic viscosity (3.80×10^{-3} cm^2 s^{-1} for 0.5 M NaCl solution at 80 °C [38]). The assumption here is of a fixed surface concentration dependent only on the electrode potential at a given pH. The current $i_{diss,n}$ represents a current that is in parallel to the dissolution current but not (in this formulation) transport dependent. In the framework of our separation of the current into a part due to dissolution and a part due to electrocrystallisation, this might be the fraction of the current during the pre-peak plateau that is consumed in growing the crystalline layer: $i_{diss,n}$ might be the current corresponding to Eq. (1) over this part of the transient. However, note that the current i_{cryst} modelled in section 3 is not constant and is significantly less than the value determined for $i_{diss,n}$. We note that in this first stage of formation of the crystalline layer, the X-ray signal was below the limit of detection so the actual variation of volume of material, V, with time, t, is unknown and the X-ray signal cannot be used to confirm or deny this hypothesis. However, the transport modelling developed in section 3.6 does not support the idea that $i_{diss,n}$ is a crystal nucleation current, since the observed values imply a flux of carbonate to the electrode surface that is much greater than can be supported. A model is that the dissolution reaction, Eq. (2) has two parts, occurring in parallel and therefore presumably spatially separated. One part is, as shown elsewhere, catalysed by bicarbonate with rate limited by transport in the solution [23]. The other part we assume un-catalysed, having rate that is independent of transport in the solution, but instead is controlled by the electrical resistance of the precursor amorphous film. The linear variation of $i_{diss,n}$ with electrode potential is consistent with this idea. It will be shown in sections 3.6 and 3.7 that the relative magnitude of the two components of the dissolution current critically impacts the dependence on solution flow rate of surface supersaturation and in consequence the kinetics of formation of the crystalline layer, which in turn would be a critical factor determining whether a protective scale ultimately forms.

From the slope of the dependence of i_{plat} on $\omega^{1/2}$ (see Fig. 7A), the surface concentration of the dissolving species can be calculated, with assumptions concerning z and D. Assuming values for Fe^{2+} ($z = 2$ and $D = 2.1 \times 10^{-5}$ cm^2 s^{-1} at 80 °C) the value of c_s comes out in the range 0.1–1 mM, varying exponentially with ($E - E_{corr}$) with slope approximately 120 mV/decade, Fig. 8. The surface concentration is just a transformation of the current density, through Eqs. (5) and (6), so should have the same Tafel dependence, as indeed appears to be the case. An apparent supersaturation, S_{app}, for $FeCO_3$ can be calculated and compared to expectations assuming that the concentration gradient of carbonate (and hence of hydrogen ions) is not large:

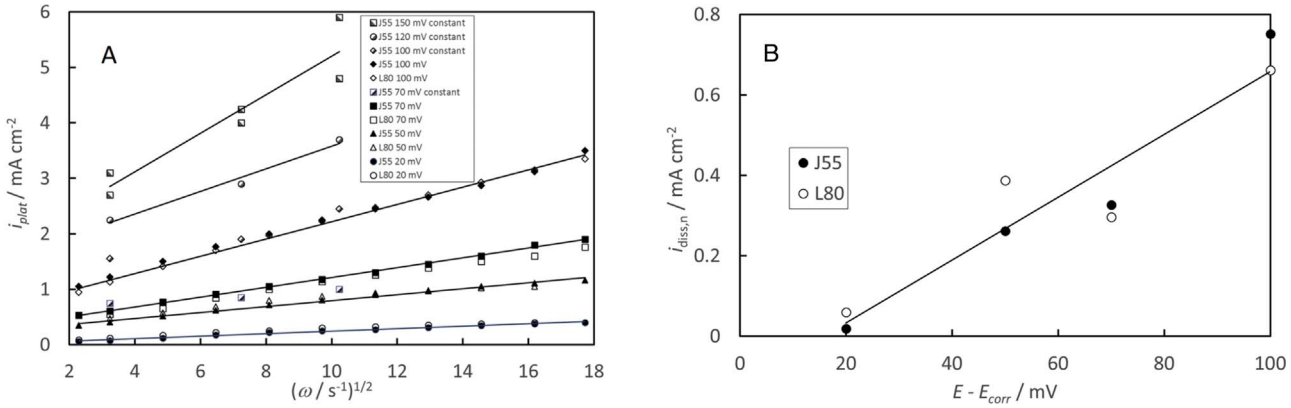

Fig. 7. (A) Levich dependence of the pre-peak plateau current: i_{plat} against ω / rad s^{-1} for two carbon steels of different microstructure: J55 and L80. (B) Dependence of intercept, $i_{diss,n}$, on electrode potential.

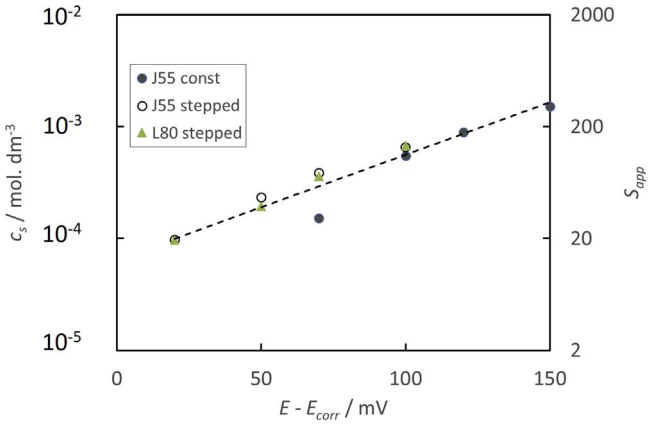

Fig. 8. Surface concentration of the dissolving species, c_s and apparent supersaturation for $FeCO_3$, S_{app} estimated from the rotation rate − dependence of i_{plat} at 80 °C in CO_2-saturated 0.5 M NaCl with pH_{calc} = 6.8. Carbon steels with two different microstructures, either individual experiments at constant rotation rate or single experiments with stepped rotation rate (see legend).

$$S_{app} = \frac{c_s [CO_3^{2-}]_{bulk}}{K_{sp}} \tag{7}$$

with solubility product, $K_{sp} = 1.37 \times 10^{-10}$ mol^2 L^{-2} [39] and $[CO_3^{2-}] = 2.7 \times 10^{-5}$ M at 80 °C with pH_{calc} = 6.8. The apparent supersaturation becomes very high (Fig. 8) which implies that the dissolving species is not Fe^{2+}. The dominant solution species at the bulk solution pH is bicarbonate, and it has been noted before that the concentration of soluble iron species near an electrode anodically dissolving in the presence of bicarbonate is much larger than that expected from the solubility of iron carbonate [22,23]. Castro et al. [22] proposed an unstable soluble bicarbonate complex of Fe(II) whilst Davies and Burstein proposed $Fe(CO_3)_2^{2-}$. A mass transport-limited dissolution rate was also proposed in those works, as here.

3.6. Model to relate current density and rotation rate to supersaturation and precipitation rate of colloid in the solution

The previous section focused on the rotation rate-dependent part of the dissolution current. The objective of this section is to set the stage for interpretation of the effects of experimental variables on the kinetics of growth of the crystalline layer. The aim is to provide a model that approximately describes the variation of supersaturation of $FeCO_3$ at the interface over the time period when current i_{cryst} is growing towards the peak. Then, in section 3.7 below, we show how the electrocrystallisation reaction is controlled by the supersaturation. In the model, the dissolution rate is expressed as the sum of two fluxes, as indicated by the results in section 3.5, above. The formation of colloidal iron carbonate removes carbonate from the region near the interface and thus alters the supersaturation. We assume iron dissolving as an Fe(II) species written for convenience as Fe^{2+} (though as we noted in section 5, the dissolving species is probably not Fe^{2+}) and a bimolecular precipitation reaction forming colloidal product and hence removing Fe^{2+} and CO_2 (as carbonate) from the solution [12]. This formulation of the precipitation rate is similar to the approach used in Van Hunnik et al. [3] but we note following [22] that the precipitation kinetics by reaction of the dissolving bicarbonate or carbonate species might be more complicated. The consumption of carbonate by precipitation of $FeCO_3$ releases hydrogen ions, which changes the local pH and hence the local concentrations of the carbon species, thus the local supersaturation and thus feeds back to the local precipitation rate. We simplified the model by ignoring effects of electromigration in view of the excess of supporting electrolyte, NaCl. We ignore the effects of pH on the precipitation rate constant.

The variation of concentration with position x normal to the interface is then in the steady state given by:

$$D_j \frac{d^2 C_j}{dx^2} - v_x \frac{dC_j}{dx} - k_p C_{Fe^{2+}} C_{CO_3} = 0 \tag{8}$$

Here, j denotes Fe^{2+}, CO_3^{2-}, or CO_2 concentration C_j and diffusion coefficient D_j, v_X is velocity normal to the interface and k_p is the bimolecular precipitation rate constant for formation of colloidal product. A convenient scaling for distance, X, normal to the interface, is the diffusion boundary layer thickness, $\delta = 1.61 D_{Fe}^{1/3} \nu^{1/6} \omega^{-1/2}$. This choice of scaling, $X = x/\delta$ where x denotes the distance away from the interface, rather conveniently includes the effects of variation of rotation rate. The axial velocity, transporting matter towards the surface, is independent of radial position. Levich [40] (page 70) points out that the diffusion boundary layer thickness is only some 5% of the total hydrodynamic boundary layer thickness so that the small-distance limiting expression for the axial velocity can therefore be used: $v_x \approx -0.51 x^2 \sqrt{\omega^3/\nu}$. The scaled velocity is therefore $V_X = v_x \delta / D = -2.13 X^2$. Thus variation of axial velocity due to variation of rotation rate has been incorporated as an effect on the distance scaling. This distance scaling, however, constrains the reaction boundary layer, within which precipitation is occurring, to be the same as the diffusion boundary layer and is thus an approximation. A convenient scaling for concentration is $\Gamma_j = C_j / C_{tot}$ where C_{tot} is the total concentration of carbon species (CO_2, H_2CO_3, HCO_3^-, CO_3^{2-}). This is conserved through the boundary layer − for each carbonate removed by precipitation, one CO_2 is supplied from the bulk of the solution. The species that are introduced to and removed from the boundary layer by irreversible reaction are Fe^{2+}, CO_3^{2-} and CO_2. All other species have concentration within the boundary layer established by chemical equilibrium. There are two limits: where the hydration rate of CO_2 is much greater than or much less than the precipitation rate. Then in the scaled variables the equations to solve (where 1 denotes Fe^{2+}, 2 denotes H^+, 3 denotes CO_3^{2-} and 4 denotes CO_2) are:

a) Equilibrium in the boundary layer

$$\frac{d^2\Gamma_1}{dX^2} + 2.13X^2 \frac{d\Gamma_1}{dX} - \frac{K_p}{\omega} \Gamma_1 \Gamma_3 = 0 \tag{9a}$$

$$\frac{d^2\Gamma_3}{dX^2} + 2.13X^2 \frac{d\Gamma_3}{dX} - \frac{K_p}{\omega} \Gamma_1 \Gamma_3 = 0 \tag{9b}$$

$$\Gamma_2 = (-K_1 \Gamma_3 + \sqrt{K_1^2 \Gamma_3^2 + 4K_2})/2 \tag{9c}$$

b) CO_2 hydration rate controlled

$$\frac{d^2\Gamma_1}{dX^2} + 2.13X^2 \frac{d\Gamma_1}{dX} - \frac{K_0}{\omega} \Gamma_4 = 0 \tag{10a}$$

$$\frac{d^2\Gamma_3}{dX^2} + 2.13X^2 \frac{d\Gamma_3}{dX} - \frac{K_0}{\omega} \Gamma_4 = 0 \tag{10b}$$

$$\frac{d^2\Gamma_4}{dX^2} + 2.13X^2 \frac{d\Gamma_4}{dX} - \frac{K_0}{\omega} \Gamma_4 = 0 \tag{10c}$$

$$\Gamma_2 = K_2 (1 - \Gamma_4)/\Gamma_3 \tag{10d}$$

Here (80 °C; saturated with CO_2 in equilibrium with water vapour at total pressure 1 bar; pH_{calc} = 6.8) $C_{tot} = 5.17 \times 10^{-2}$ M and the scaled equilibrium constants are $K_2 = 6.17 \times 10^{-9}$; $K_1 = 1.49 \times 10^{-5}$. The hydration rate constant [41] when scaled is $K_0 = 1.33\ s^{-1}$. The boundary conditions are: $(d\Gamma_1/dX)_{X=0}$ fixed at the experimental values, $J = i_{plat}\delta/FDC_{tot}$; $(\Gamma_1)_{X=1} = 0$; $(\Gamma_3)_{X=1}$ and $(\Gamma_4)_{X=1}$ are the scaled bulk CO_3^{2-} and CO_2 concentrations (1.70×10^{-3} and 0.168 respectively) and the gradients $(d\Gamma_3/dX)_{X=0}$. and $(d\Gamma_4/dX)_{X=0} = 0$. Diffusion coefficients are all taken equal to D_{Fe}. The scaled precipitation rate constant, K_p, which here has units s^{-1} to account for the dependence of the distance scaling on rotation rate, ω, is unknown. It will be zero for some supersaturation less than a critical supersaturation.

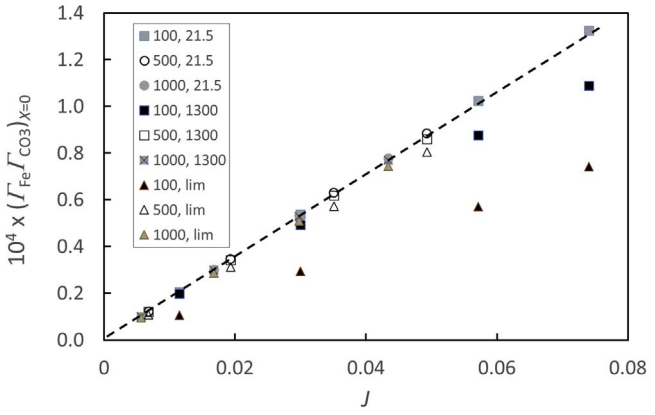

Fig. 9. Calculated scaled surface concentration product of iron and carbonate: dependence on experimental surface flux, $J = \frac{i_{plat}\delta}{2FDc_{tot}}$ for different values of rotation rate / rpm and precipitation rate constant, K_p (legend: ω, K_p). The limit case is for rate controlled by the hydration rate of CO_2.

However, we have not introduced that complexity (and additional parameter) into the present discussion. Eqs. (9) and (10) were solved numerically (Matlab) to give the scaled concentration product $(\Gamma_1\Gamma_3)_{X=0} = C_{Fe}C_{CO_3}/C_{tot}^2$ and the flux $J = (dC_{Fe}/dX)_{X=0}$ for a range of K_p and ω: Fig. 9. The problem of not knowing K_p is resolved by noting that these curves all approximately fell onto a common line unless ω was low and K_p large. Hence an adequate empirical relationship for the surface concentration product as a function of the flux (proportional to the product of the current density and the diffusion boundary layer thickness) can be given, assuming that K_p is not too large. Thus, for each experiment, the concentration product $(\Gamma_1\Gamma_3)$ $X = 0$ before the peak could be calculated.

The apparent supersaturation corresponding to the calculated values of the concentration product, $S'_{app} = (\Gamma_1\Gamma_3)_{X=0}(C_{tot})^2/K_{sp}$ is very high, as would be apparent also from Fig. 8. In section 3.7 we show that the variation of S'_{app} with experimental conditions, which we assume corresponds to the variation of the actual supersaturation, systematizes and explains the data for variation of the electrocrystallisation rate. The calculated surface pH was ~5.4 for most conditions (bulk pH 6.8).

3.7. Crystallisation kinetics: dependence on supersaturation

Fig. 10 shows that the significant change in rate of formation of a crystalline layer (as measured by the time to reach the current peak as previously discussed in Section 2) with change of conditions − e.g. change of rotation rate illustrated in Fig. 2 − is simply accounted for by the dependence of crystallization rate on apparent supersaturation calculated from Fig. 9. The dependence follows the form often assumed and observed [8]: quadratic for low rates (here $pH_{calc} = 6.8$) and linear for high rates (here $pH_{calc} = 7.3$) [4,42]. The supersaturation is controlled by the current density flowing in the pre-peak plateau region, which is in turn controlled by the thickness of the amorphous layer present there, and by the diffusion boundary layer thickness. The counter-intuitive result is that, with increase of rotation rate at constant electrode potential, the supersaturation decreases although the dissolution current increases: this is the effect that accounts for the decrease in crystallization rate constant that causes the increase in time to the current peak. The variation in S_{app} that systematizes variation in crystallization rate constant arises from the contribution of the rotation rate-independent term in the dissolution current, $i_{diss,n}$.

Given the experimental result (Eq. (5)) and the results of section 6, the surface flux and therefore surface saturation can be described as:

$$J = \text{constant}\times(k_m + i_{diss,n}\omega^{-1/2}) \quad \text{and} \quad S'_{app} \sim \text{constant}\times(k_m + i_{diss,n}\omega^{-1/2}) \tag{11}$$

The effect of the rotation rate-independent dissolution current contribution $i_{diss,n}$ is that the higher the rotation rate, the smaller is the supersaturation driving crystal growth. Unsurprisingly, this leads to better formed crystals on the surface (Fig. 2). The reaction paths are illustrated schematically in Fig. 11.

The much smaller crystallization rates observed in the restricted geometry of the synchrotron cell signal much lower supersaturations in this cell than in the laboratory rotating disc cell. The low supersaturation in the synchrotron cell would be because of the long diffusion path for carbon dioxide: this species would be efficiently consumed by the precipitation reaction in the space above the electrode. The gradient of CO_2 concentration becomes large when K_p is large and the mass-transfer rate to the electrode surface is small so in this sense the nucleation and crystal growth rate of a crystalline scale are controlled by the precipitation rate of colloidal material.

The significant effects of increasing surface roughness in increasing the crystallisation rate noted previously [14] were reproduced and these effects became apparently more pronounced at higher rotation rate (Fig. S5). The effects of surface roughness caused by polishing with different size abrasives on mass transport to a rotating disc electrode have been discussed [43]. If surface scratch depths were less than about 10% of the diffusion boundary layer thickness then the Levich constant, evaluated using the geometric current density (current/geometric area) was hardly affected even though the actual current could be increased by a factor of up to 4 times as a consequence of the increased real area. Diffusion boundary layer thickness in the present work, calculated

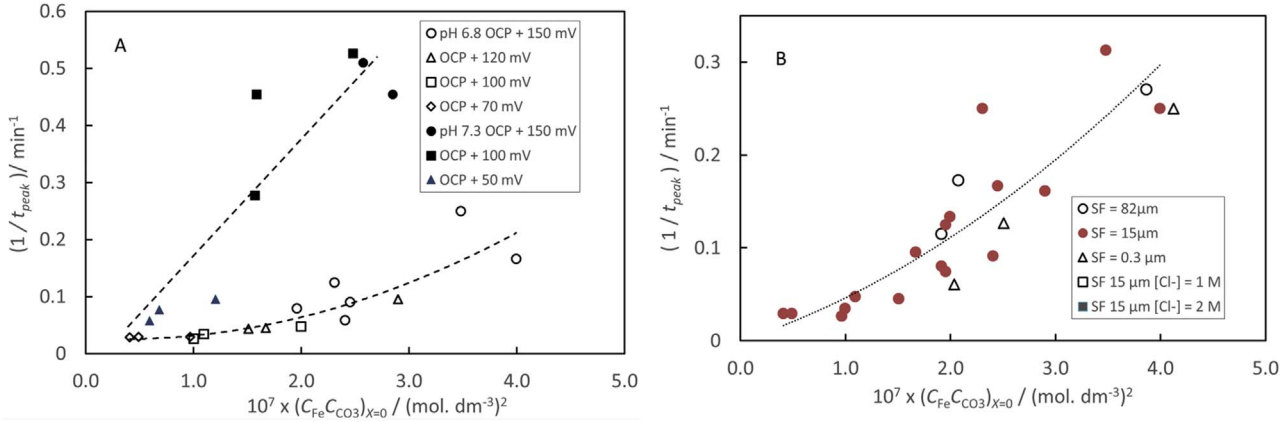

Fig. 10. Dependence of crystallization rate constant, measured as reciprocal time to the current peak, $1/t_{peak}$, upon surface concentration product, calculated from the pre-peak plateau current density per unit geometric area, i_{plat} for various rotation rates and electrode potentials (A) effect of solution pH_{calc}. (B) effect of surface roughness (final abrasive particle size) and chloride concentration at $pH_{calc} = 6.8$. CO_2–saturated solution, 0.5 M NaCl unless otherwise stated, 80 °C. The lines show a quadratic dependence of crystal growth rate constant on concentration product at $pH_{calc} = 6.8$ and linear at $pH_{calc} = 7.3$.

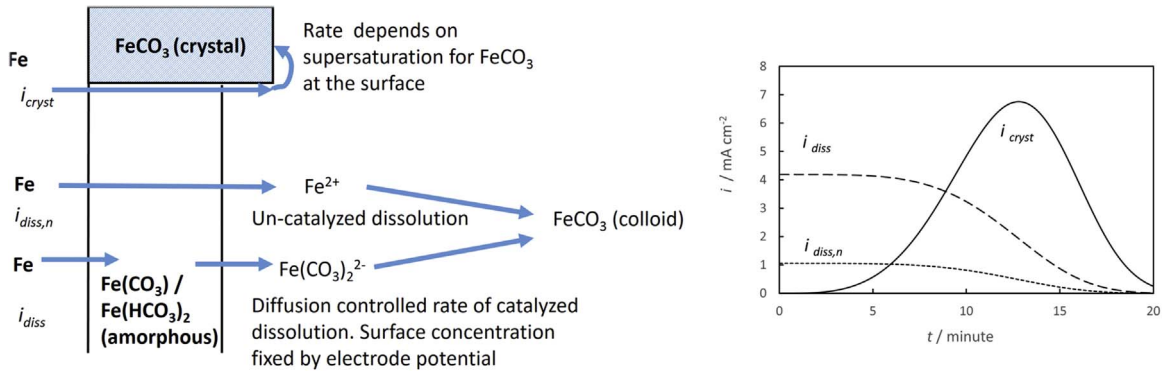

Fig. 11. Schematic representation of the processes at the interface. A: phases − amorphous precursor film, growing crystals and precipitate in solution. B: components of the current density: catalyzed dissolution, i_{diss}, diffusion controlled with Tafel dependence on electrode potential; un-catalysed dissolution, $i_{diss,n}$, flow independent, linearly dependent on electrode potential; crystal growth, i_{cryst}, dependent on supersaturation at the interface.

using the diffusion coefficient for Fe^{2+}, would vary from 54 μm at 100 rpm to 17 μm at 1000 rpm. Some effect of the very coarse abrasive at high rotation rate on the mass transport and hence the surface supersaturation might be expected, but Fig. 10 shows that, within the experimental uncertainty and the assumptions made in the modelling calculation, the effect of surface roughness is simply accounted for by the effect of the increased area giving an increase in i_{plat} and hence an increased surface supersaturation. Fig. 10 also shows a negligible effect of NaCl concentration, in the range 0.5–2 M.

3.8. Deductions concerning the importance of microenvironments and the chemistry of dissolution and reaction of the first-formed amorphous layer

In this work, we have developed further the idea that siderite forms by transformation of a thin, amorphous surface layer that is the initial corrosion product. The current peak signaling the covering of the surface by crystalline siderite is simply interpreted as a current consumed by the direct electrochemical formation of crystals. Previously, we have interpreted the current rise as either an effect of a local change of pH [11,12] or as the effect of crystal growth consuming the amorphous material and causing a local thinning of the amorphous layer [12], but the present interpretation seems quite adequate. The work emphasizes the importance of this amorphous initial layer in controlling the current density which drives the subsequent development of a crystalline scale. The dissolution chemistry and the detailed chemical composition of this layer is worthy of further study, for this might explain factors such as the significant effects of trace organic acids on crystalline scale formation. The importance of microenvironments has been raised in other work [36,37]. Here, we have shown just how sensitive to small changes in pH is the crystallization rate and the ratio of chukanovite to siderite, and have deduced that chukanovite follows siderite in the crystallization chain. The consumption of CO_2 caused both by precipitation of colloidal material which is the product of the dissolution reaction and also by the crystal growth causes a decrease in pH near the interface. As noted in section 3.6, we calculated a surface pH ~ 5.4 for bulk pH = 6.8. The change would be larger in restricted microenvironments and even more so if the precipitation rate and crystal growth rate significantly exceed the hydration rate of CO_2: an effect which we have in earlier work indicated as potentially significant [11]. Local formation of chukanovite in such environments is feasible [36] as is transformation of the first-formed siderite to chukanovite. Chukanovite scales are plate-like rather than cubic and it seems plausible that they would be less protective. Thus, the pH-dependence of crystallization rate and crystal form, and change of pH caused by crystallization and by formation of the colloidal product of the dissolution reaction might offer an interpretation for initiation of localized corrosion. Certainly, the sensitivity of crystal growth rate to mass transport conditions demonstrated in the present work points to the significance of microenvironments to which transport is restricted as places where scale formation will be significantly altered. The relative contributions of the transport-dependent ('catalysed') and transport-independent ('un-catalysed') components of the current, which are electrode potential-dependent, are also important, as shown in section 3.7. Since the part of the supersaturation due to the 'un-catalysed' current decreases with increasing mass-transport rate (Eq. (11)), it causes a decrease in crystal growth rate despite the total dissolution current increasing. Together with the effects of pH change near the surface, this raises the possibility that spatial variations in mass-transport rate might amplify a spatial instability in the corrosion rate, leading to localized corrosion.

Acknowledgement

This work was supported by: the Qatar National Research Fund, contract NPRP 7 − 146 − 2–072; New Zealand Ministry of Business, Innovation and Employment, contract CO8X1003; The New Zealand Synchrotron Group Ltd; and the MacDiarmid Institute for Advanced Materials and Nanotechnology, NZ. Thanks also to Nick Birbilis (Monash University) for his generous advice and loan of equipment, to Erich Kisi (University of Newcastle, Australia) for the use of the VHR detector, and to Bijan Kermani and Tenaris Ltd for the gift of pipeline steel. Portions of this research were undertaken on the Powder Diffraction beam line at the Australian Synchrotron, Victoria, Australia. The views expressed herein are those of the authors and are not necessarily those of the owner or operator of the Australian Synchrotron.

Appendix A. Supplementary data

Supplementary data associated with this article can be found, in the online version, at http://dx.doi.org/10.1016/j.corsci.2017.05.026.

References

[1] M. Kermani, A. Morshed, Carbon dioxide corrosion in oil and gas production-A compendium, Corrosion 59 (2003) 659–683.
[2] R.C. Woollam, S. Hernandez, Assessment and comparison of CO_2 corrosion prediction models, 2006 SPIE International Oilfield Corrosion Symposium, Society of Petroleum Engineers, Aberdeen, Scotland, 2006.
[3] E.W.J.V. Hunnik, B.F.M. Pots, E.L.J.A. Hendriksen, The formation of protective $FeCO_3$ corrosion product layers in CO_2 corrosion, Paper No. 6, CORROSION/96, NACE International, 1996.
[4] S. Nešić, M. Nordsveen, R. Nyborg, A. Stangeland, A mechanistic model for carbon dioxide corrosion of mild steel in the presence of protective iron carbonate Films—Part 2: a numerical experiment, Corrosion 59 (2003) 489–497.
[5] M. Nordsveen, S. Nešić, R. Nyborg, A. Stangeland, A mechanistic model for carbon dioxide corrosion of mild steel in the presence of protective iron carbonate Films—Part 1: theory and verification, Corrosion 59 (2003) 443–456.
[6] E. Remita, B. Tribollet, E. Sutter, F. Ropital, X. Longaygue, J. Kittel, C. Taravel-Condat, N. Desamais, A kinetic model for CO_2 corrosion of steel in confined aqueous environments, J. Electrochem. Soc. 155 (2008) C41–C45.
[7] S. Nesic, K.-L.J. Lee, V. Ruzic, A mechanistic model of iron carbonate film growth and the effect on CO_2 corrosion of mild steel, Paper No: 237, CORROSION/02,

NACE International, 2002.
[8] M.L. Johnson, M.B. Tomson, Ferrous carbonate precipitation kinetics and its impact CO_2 corrosion, Paper No. 268, CORROSION/91, NACE International, 1991.
[9] A. Dugtad, The importance of $FeCO_3$ supersaturation on the CO_2 corrosion of carbon steels, Paper No. 14, CORROSION/92, NACE International, 1992.
[10] B. Ingham, M. Ko, G. Kear, P. Kappen, N. Laycock, J.A. Kimpton, D.E. Williams, In situ synchrotron X-ray diffraction study of surface scale formation during CO_2 corrosion of carbon steel at temperatures up to 90 °C, Corros. Sci. 52 (2010) 3052–3061.
[11] B. Ingham, M. Ko, N. Laycock, J. Burnell, P. Kappen, J.A. Kimpton, D.E. Williams, In situ synchrotron X-ray diffraction study of scale formation during CO_2 corrosion of carbon steel in sodium and magnesium chloride solutions, Corros. Sci. 56 (2012) 96–104.
[12] B. Ingham, M. Ko, N. Laycock, N.M. Kirby, D.E. Williams, First stages of siderite crystallisation during CO_2 corrosion of steel evaluated using in situ synchrotron small- and wide-angle X-ray scattering, Faraday Discuss. 180 (2015) 171–190.
[13] M. Ko, B. Ingham, N. Laycock, D.E. Williams, In situ synchrotron X-ray diffraction study of the effect of chromium additions to the steel and solution on CO_{2c}orrosion of pipeline steels, Corros. Sci. 80 (2014) 237–246.
[14] M. Ko, B. Ingham, N. Laycock, D.E. Williams, In situ synchrotron X-ray diffraction study of the effect of microstructure and boundary layer conditions on CO_2 corrosion of pipeline steels, Corros. Sci. 90 (2015) 192–201.
[15] M. Ko, N.J. Laycock, B. Ingham, D.E. Williams, In situ synchrotron X-Ray diffraction studies of CO_2 corrosion of carbon steel with scale inhibitors ATMPA and PEI at 80 °C, Corrosion 68 (2012) 1085–1093.
[16] M.T. Alam, E.W.L. Chan, R. De Marco, Y. Huang, S. Bailey, Understanding complex electrochemical impedance spectroscopy in corrosion systems using in-situ synchrotron radiation grazing incidence X-ray diffraction, Electroanalysis 28 (2016) 2166–2170.
[17] C.d. Waard, U. Lotz, D.E. Milliams, Predictive model for CO_2 corrosion engineering in wet natural gas pipelines, Corrosion 47 (1991) 976–985.
[18] A. Dugstad, L. Lunde, K. Videm, Parametric study of CO_2 corrosion of carbon steel, Nace, International, Houston TX (United States), 1994.
[19] T. Hara, H. Asahi, Y. Suehiro, H. Kaneta, Effect of flow velocity on carbon dioxide corrosion behavior in oil and gas environments, Corrosion 56 (2000) 860–866.
[20] F. de Moraes, J.R. Shadley, J. Chen, E.F. Rybicki, Characterization of CO_2 corrosion product scales related to environmental conditions, Corrosion 2000, NACE International, 2000.
[21] S. Nešić, G.T. Solvi, J. Enerhaug, Comparison of the rotating cylinder and pipe flow tests for flow-sensitive carbon dioxide corrosion, Corrosion 51 (1995) 773–787.
[22] E.B. Castro, J.R. Vilche, A.J. Arvia, Iron dissolution and passivation in K2CO3-KHCO3 solutions. rotating ring disc electrode and XPS studies, Corros. Sci. 32 (1991) 37–50.
[23] D. Davies, G. Burstein, The effects of bicarbonate on the corrosion and passivation of iron, Corrosion 36 (1980) 416–422.
[24] P. Southworth, A. Hamnett, A.M. Riley, J.M. Sykes, An ellipsometric and rrde study of iron passivation and depassivation in carbonate buffer, Corros. Sci. 28 (1988) 1139–1161.
[25] R.G. Bates, V.E. Bower, Standard potential of the silver-silver-chloride electrode from 0 to 95C and the thermodynamic properties of dilute hydrochloric acid solutions, J. Res. Nat. Bur. Stand 53 (1954) 283–290.
[26] F.G. Baucke, Thermodynamics of solid-state connected ion-sensitive membrane electrodes: the silver-silver chloride system: part II. Standard potentials between 5 and 90 °C of the 2nd kind silver-silver chloride reference electrode with 3.5 M and sat'd KCl measured by means of membrane electrodes, J. Electroanal. Chem. Interfacial Electrochem. 67 (1976) 291–299.
[27] B. Ingham, Statistical measures of spottiness in diffraction rings, J. Appl. Crystallogr. 47 (2014) 166–172.
[28] J.C. Taylor, I. Hinczak, Rietveld Made Easy: a Practical Guide to the Understanding of the Method and Successful Phase Quantifications, Sietronics Pty Limited, 2006.
[29] B.E. Warren, X-ray Diffraction, Dover Publications, New York, 1990.
[30] A. Riley, J. Sykes, The active—passive transition in low alloy steels in carbonate solutions, Electrochim. Acta 35 (1990) 35–45.
[31] J. Blengino, M. Keddam, J. Labbe, L. Robbiola, Physico-chemical characterization of corrosion layers formed on iron in a sodium carbonate-bicarbonate containing environment, Corros. Sci. 37 (1995) 621–643.
[32] A.K. Grzybowski, The standard potential of the calomel electrode and its application in accurate physicochemical measurements. 1. The standard potential, J. Phys. Chem. 62 (1958) 550–555.
[33] M. Avrami, Kinetics of phase change. II: transformation-time relations for random distribution of nuclei, J. Chem. Phys. 8 (1940) 212–224.
[34] A. Bewick, H.R. Thirsk, M. Fleischmann, Kinetics of electrocrystallization of thin films of calomel, Trans. Faraday Soc. 58 (1962) (2200- &).
[35] M. Fleischmann, J.A. Harrison, H.R. Thirsk, Electrocrystallization of thin films of nickel, Trans. Faraday Soc. 61 (1965) 2742-.
[36] V. Pandarinathan, K. Lepkova, W. van Bronswijk, Chukanovite ($Fe_2(OH)_2CO_3$) identified as a corrosion product at sand-deposited carbon steel in CO_2-saturated brine, Corros. Sci. 85 (2014) 26–32.
[37] W. Liu, J.J. Dou, S.L. Lu, P. Zhang, Q.H. Zhao, Effect of silty sand in formation water on CO_2 corrosion behavior of carbon steel, Appl. Surf. Sci. 367 (2016) 438–448.
[38] J. Kestin, H.E. Khalifa, R.J. Correia, Tables of the dynamic and kinematic viscosity of aqueous NaCl solutions in the temperature-Range 20–150 °C and the pressure range 0.1–35 MPa, J. Phys. Chem. Ref. Data 10 (1981) 71–87.
[39] W. Sun, S. Nešić, R.C. Woollam, The effect of temperature and ionic strength on iron carbonate ($FeCO_3$) solubility limit, Corros. Sci. 51 (2009) 1273–1276.
[40] V.G. Levich, Physicochemical Hydrodynamics, Prentice Hall, 1962.
[41] A.L. Soli, R.H. Byrne, CO_2 system hydration and dehydration kinetics and the equilibrium CO_2/H_2CO_3 ratio in aqueous NaCl solution, Mar. Chem. 78 (2002) 65–73.
[42] J.W. Mullin, Crystallization, Elsevier Science, Jordan Hill, 2001.
[43] S. Bruckenstein, J.W. Sharkey, J.Y. Yip, Effect of polishing with different size abrasives on the current response at a rotating-disk electrode, Anal. Chem. 57 (1985) 368–371.